Materials Horizons

ROYAL SOCIETY OF CHEMISTRY

COMMUNICATION

View Article Online
View Journal | View Issue

Cite this: *Mater. Horiz.*, 2025, 12, 4685

Received 8th March 2025,
Accepted 15th April 2025

DOI: 10.1039/d5mh00416k

rsc.li/materials-horizons

Catalytic methane dissociation and its non-oxidative coupling in metal-dispersed molten salt media: an *ab initio* molecular dynamics investigation†

Pritam Rudra, [a] Ojus Mohan *[a] and Samir H. Mushrif *[b]

Methane dehydrogenation ($CH_{4(g)} \rightarrow C_{(s)} + 2H_{2(g)}$) in molten media is an emerging technology to produce CO_2-free hydrogen and solid carbon. However, molten salts exhibit little catalytic activity for methane dissociation. In this study, we propose a catalytically active solid metals dispersed molten salt for the non-oxidative dehydrogenation of methane, investigating both the sequential dehydrogenation of methane and its non-oxidative coupling, which can produce more valuable C_2 products over solid carbon. Four different solid metals, namely, nickel, boron-doped nickel, copper, and boron-doped copper are investigated for their activity, stability against coking, and selectivity towards C_2 products in the molten sodium bromide (NaBr) salt. The catalytic reactions in the explicit condensed phase, with finite temperature effects are studied using *ab initio* molecular dynamics (AIMD) and metadynamics simulations at 1200 K. Our investigation demonstrated that at high temperatures, microstructural changes in the Cu catalyst are more pronounced than those in the Ni catalyst, enhancing the activity of Cu significantly. Moreover, these *operando* structural changes in the catalyst at high temperatures can only be captured by AIMD simulations, and not by ground-state DFT calculations. Our calculated free energy barriers for methane dehydrogenation indicate that boron doping in Ni and Cu catalysts lowers the CH_4 activation barrier by 39 kJ mol^{-1} and 60 kJ mol^{-1}, respectively in comparison with Ni catalysts. Furthermore, we found that the CuB–NaBr system kinetically promotes non-oxidative C–C coupling reactions over the competing dehydrogenation of CH_x intermediates, whereas other metal-dispersed systems primarily favor complete CH_4 dehydrogenation to form carbon. Interestingly, the carbon generated as a byproduct diffuses into Ni and Cu, leading to deactivation, but boron-doped systems prevent this diffusion, making them promising candidates that are stable against catalyst deactivation. Moreover, we have not observed any leaching of metal atoms from the catalyst into the molten salt medium, nor the diffusion of boron from the subsurface to the on-the-surface at these elevated temperatures, ensuring the stability of the system under these conditions. This first-principles-based study revealed that heterogeneous catalysts in molten salts have the potential to catalyse the non-oxidative dehydrogenation of CH_4, and that boron-doped Cu in molten NaBr is a promising system for non-oxidative C–C coupling reactions.

New concepts

Using *ab initio* molecular dynamics with biasing techniques, we provide a first-of-its-kind study of methane dehydrogenation and C–C coupling reactions in a condensed-phase molten salt system with dispersed metals, revealing unique catalytic behavior inaccessible to conventional approaches. This simulation method explicitly accounts for finite-temperature effects, including the dynamic behavior of the molten medium, catalyst microstructural transformations, and reactant-catalyst interactions. These critical aspects are inaccessible through conventional ground-state DFT calculations and remain extremely challenging to probe experimentally. Our findings reveal that dispersing active metals in an inert molten salt significantly lowers the methane activation barrier, enhancing catalytic performance. Furthermore, boron doping in the dispersed metals further lowered the activation barrier, showcasing its effectiveness in enhancing catalytic performance. Notably, this study is the first to explore boron-doped metals in molten salts at high temperatures. A systematic analysis of coke formation and catalyst stability under high-temperature conditions shows strong agreement with experimental data, reinforcing the reliability of our simulations. Interestingly, while most metal-dispersed systems favor complete methane dehydrogenation, CuB–NaBr uniquely promotes C–C coupling, showing potential for forming more valuable C_2 chemicals. By demonstrating how molten-phase environments influence reaction kinetics and selectivity, our work introduces a new framework for designing catalysts for methane valorization.

[a] *Department of Chemical Engineering, Indian Institute of Technology Bombay, Powai, Mumbai, Maharashtra 400076, India. E-mail: ojus@iitb.ac.in*

[b] *Department of Chemical and Materials Engineering, University of Alberta, 9211-116 Street Northwest, Edmonton, Alberta T6G 1H9, Canada. E-mail: mushrif@ualberta.ca*

† Electronic supplementary information (ESI) available: S1. Metadynamics calculated free energy reaction profiles for the (i) dehydrogenation of CH_3 to CH_2, (ii) dehydrogenation of CH_2 to CH, (iii) dehydrogenation of CH to C, and (iv) the CH–CH coupling reaction in Ni–NaBr, NiB–NaBr, Cu–NaBr, and CuB–NaBr metal-molten media systems, S2. Car–Parrinello molecular dynamics and metadynamics sample input file, S3. Plot of fictitious electronic kinetic energy *vs.* time during the equilibration of the first dehydrogenation reaction, S4. Optimisation of K-point grid S5. Variation of distance over time between the carbon and the top Cu layer, S6. Comparison of free energy barriers of all reactions, with previously reported works. See DOI: https://doi.org/10.1039/d5mh00416k

1. Introduction

In recent years, natural gas has gained prominence as a sustainable and cost-effective source of hydrocarbons, with significant potential to replace coal and crude oil in various energy sectors and chemical industries.[1,2] Natural gas is primarily composed of methane, with smaller amounts of other hydrocarbons and impurities like sulfur compounds. Conventional methods like steam methane reforming (SMR) for methane conversion face challenges such as substantial CO_2 emissions, significant exergy loss, and high capital costs due to the complexity and multistage nature of the processes.[3,4] Alternatively, methane can be directly converted through oxidative coupling or non-oxidative dehydrogenation to produce valuable products that have attracted significant attention. Essentially all such direct methane conversion processes rely on the dehydrogenation of methane. Methane has a regular tetrahedral structure with four identical C–H σ bonds formed through sp^3 hybridization, each bond having an energy of up to 435 kJ mol^{-1}.[5,6] The strong C–H bonds and non-polarity make CH_4 decomposition difficult, posing a challenge for methane pyrolysis. At high temperatures (>1200 °C), methane undergoes thermal decomposition without a catalyst, producing CH_3 radicals through homogeneous C–H bond cleavage.[7,8] At temperatures below 1100 °C without a catalyst, the reaction rate is slow, resulting in very poor CH_4 conversion.[5] In the oxidative coupling of methane (OCM) process, methane is activated with the aid of oxygen, and the presence of a catalyst lowers the reaction temperature. However, the OCM process has several drawbacks, including the presence of O_2 causing irreversible overoxidation and producing significant amounts of thermodynamically more stable end products like CO_2 and H_2O.[9,10] Interestingly, non-oxidative methane dehydrogenation (eqn (1)) enables the possibility of producing CO_2-free hydrogen from natural gas.[11,12]

$$CH_{4(g)} \rightarrow C_{(s)} + 2H_{2(g)} \quad \Delta H^0_{298K} = 74.85 \text{ kJ mol}^{-1} \text{ of } CH_4 \tag{1}$$

Additionally, methane cracking requires less energy input compared to SMR.[12] In contrast to SMR, which generates CO_2, methane dehydrogenation offers an attractive route for H_2 production, with solid carbon as a by-product. Recently a techno-economic study showed that the levelized cost for H_2 production from methane dehydrogenation ($1.75 per kg of H_2) is lower than the conventional steam methane reforming process coupled with carbon capture and sequestration technique ($1.95 per kg of H_2).[13] More importantly, in the presence of an appropriate catalyst, methane dehydrogenation can potentially produce C_2 hydrocarbons through the non-oxidative coupling of intermediates formed during the sequential dehydrogenation of methane.[14] C_2 products hold significantly higher value compared to solid carbon because they serve as essential chemical feedstocks and as energy-dense fuels. However, the non-oxidative coupling of various intermediates during the sequential dehydrogenation of methane is thermodynamically unfavorable.[15,16] Karakaya *et al.* showed that the equilibrium direct conversion of methane to C_2H_4 or C_2H_6 under non-oxidative conditions is thermodynamically limited and only favored at high temperatures.[16] Therefore, to promote C–C coupling, it is essential to kinetically inhibit the complete dehydrogenation of methane.

It is reported in the literature that various active transition metal catalysts, such as Ni, Ru, Pd, Pt, and Fe, have been extensively studied to lower the activation barrier of methane cracking.[17–20] Generally, rapid chemisorption of methane, followed by subsequent dehydrogenation, occurs on these solid catalyst surfaces. However, these catalysts are readily deactivated due to the coke deposition on the active sites of the catalyst.[21,22] The regeneration of the deactivated catalyst involves oxidizing the carbon layer present on the catalyst surface, which leads to the generation of undesirable CO_2.[23,24] Microstructural modifications, such as doping with noble metals or other transition metals, are being investigated to improve the catalyst's stability. However, adding promoters to mitigate catalyst deactivation can impact its activity, making significant breakthroughs difficult to achieve.[12,25] Additionally, Guo *et al.* reported that atomic Fe sites embedded in a silica matrix result in high catalytic selectivity for the non-oxidative conversion of methane to ethylene, aromatics, and hydrogen.[9] It has been observed that the lack of metal ensembles inhibits C–C coupling and coking, resulting in long-term stability under high-temperature reaction conditions.[9] Xie *et al.* studied non-oxidative C–C coupling during methane dehydrogenation and revealed that single-atom catalysts significantly outperformed metallic nanoparticles.[26] These catalysts achieved methane conversion of 14.1% at 975 °C with a C_2 selectivity (ethane, ethylene, and acetylene) of 74.6%.[26] To address these catalytic challenges, the non-oxidative decomposition reactions of methane in molten media is a promising method to produce H_2 and other valuable products. In molten media-based bubble column reactors, CH_4 dehydrogenation primarily occurs at the gas–liquid bubble interface, and the carbon is transported to the top of the column due to density differences, where it can be separated, and the liquid medium at the bubble surface is continuously renewed.[27,28] Additional benefits encompass enhanced heat transfer facilitated by the high heat capacity of molten media, as well as enhancement of gas residence time resulting from the viscosity of the liquid. Hence, the selection of melt is crucial and is the current focus of the research community for commercializing this process. It has been reported in the literature that various molten metals serve as effective reaction media for methane dehydrogenation reactions.[12] For example, molten metal alloys such as Ni–Bi,[28] Cu–Bi,[27] NiMo–Bi,[29] Ni–Sn,[30] *etc.* have been demonstrated as active catalysts for methane dehydrogenation. Although these molten metals are active for the methane dissociation reaction, they have several drawbacks, such as high melting points, high vapor pressure, and carbon contamination from the metal.[12,28] For example, in the case of Ni–Bi alloy, Rahimi *et al.* found 83 wt% metal contamination in the carbon.[31] To overcome these limitations, molten salts can be used as a potential alternative to molten metals for methane dissociation.[12] Molten salts possess several advantages over molten metal such as lower vapor pressure, cheaper, and less carbon contamination. Generally, single-component molten salts are weak catalysts for methane cracking. For instance, the observed apparent activation energy of molten NaBr for the methane decomposition

reaction was determined to be 295 kJ mol^{-1},[32] significantly higher than the activation barrier seen with solid transition metal catalysts. To enhance the catalytic activity of the molten salt, various techniques such as binary molten salt mixtures, dispersion of active metals into the salt, *etc.* can be employed for methane dehydrogenation reactions. Recently, various molten salt mixtures have been used to investigate the methane dehydrogenation reaction.[12,33] Molten salt mixtures such as $MnCl_2$–KCl,[33] $FeCl_3$–NaCl–KCl,[34] NaBr–KBr,[35] *etc.* have been exhibited as catalytically active molten salt mixtures for methane cracking. Alternatively, to enhance the catalytic activity of molten salts various solid metals can also be dispersed into molten salts. Patzschke *et al.* have screened various solid metal catalysts (containing La, Ni, Co, and Mn) suspended in a mixture of 51.3 mol% molten NaBr and 48.7 mol% KBr.[36] They found that Co–Mn alloy or Co catalysts are promising catalysts in the NaBr/KBr salt system for methane pyrolysis. They conducted kinetic experiments at 1000 °C in a 250 mm long quartz bubble column reactor, and the concentration of species was measured using a mass spectrometer.[36] Tarazkar *et al.* studied the properties of methane and carbon adsorbed at the interface of molten NaBr and Ni(111) using *ab initio* molecular dynamics simulations.[37] They discovered that the presence of the molten NaBr film affects the properties of the Ni(111) surface in several intriguing ways. These findings encourage use of the metal-dispersed molten salt system for methane dehydrogenation reactions. Furthermore, to favor the C–C coupling reaction pathway over the sequential dehydrogenation of methane, one strategy is to use solid transition metal catalysts for the non-oxidative dehydrogenation of methane. However, active metals in the molten media can get deactivated due to the carbon diffusion in the dispersed metals. Therefore, it is crucial to investigate the carbon diffusion in metals and their deactivation before selecting potential candidates for methane dehydrogenation and coupling.

First-principles-based computational modeling tools like density functional theory (DFT) are powerful tools for gaining deeper insights into the electronic structure, reaction mechanisms, and activity/selectivity of catalysts. To study the condensed phase reactive system, *ab initio* molecular dynamics (AIMD) simulation is an effective tool that combines DFT with finite temperature dynamics. AIMD simulations overcome the limitations arising from the uncertainties associated with empirical potentials in classical MD simulations. It is also reported in the literature that the presence of an explicit condensed phase in a catalytic system has several effects such as altering the reaction rates and mechanisms, product selectivity, catalyst stability, and durability.[38–41] The study by Bonati *et al.* serves as a crucial proof-of-concept, demonstrating that reaction mechanisms can be highly dependent on the reaction conditions.[42] It emphasizes the importance of evaluating the system's dynamics under industrially relevant conditions to gain molecular insights. Tarazkar *et al.* discovered that the presence of molten NaBr on the Ni(111) surface leads to an increase in the concentrations of Na^+ and Br^- ions at the interface.[37] Additionally, they observed a transfer of negative charge from Br^- ions at the interface to the Ni(111) surface.[37] Therefore, it is crucial to consider the complex physicochemical interactions among the condensed phase and the reactants, intermediates, products, and catalysts. However, several studies reported in the literature modeled the liquid medium as a 'glassy' solid configuration, obtained from AIMD simulations. The activation barrier of the reaction is then determined using ground-state DFT simulations.[27,32,43,44] Although activation barriers calculated from this technique offer valuable insights into the reaction mechanism, they overlook crucial dynamical factors, such as configurational changes in the catalyst structure, the degrees of freedom and dynamics of the condensed medium, and molecular vibrations. These effects are particularly significant at high temperatures. In this regard, AIMD simulations can effectively capture the finite temperature effects on the catalyst structure, reaction intermediates, and the dynamic behavior of the molecules in the condensed phase during the reaction.

However, to the best of our knowledge, no one has studied the non-oxidative methane dehydrogenation reactions in a condensed phase employing the first-principles-based AIMD simulation methods.

Hence, in the current study, we have investigated the non-oxidative dissociation of methane as well as the non-oxidative coupling of methylidene (CH_2) and methyne (CH) intermediates in metal-dispersed molten salt systems using AIMD simulations. NaBr, a catalytically weak alkali halide salt was taken as a molten salt medium for this study. Four different solid metals, *viz.*, nickel (Ni), boron-doped nickel (NiB), copper (Cu), and boron-doped copper (CuB) are dispersed into the molten NaBr salt. We have chosen these metals because they have been shown to activate CH_4, and their melting points are higher than that of NaBr (747 °C). We have studied the activity, selectivity, and stability of metals within the condensed-phase environment of the molten salt. To the best of our knowledge, the computational study of non-oxidative dissociation of methane as well as non-oxidative C–C coupling in a condensed-phase catalytic system has not been conducted before. The details of the simulation system and computational methods are provided in Section 2, while the findings from the AIMD simulation are reported in Section 3. Mechanistic insights gained from this study will assist in the development of stable and active metal-dispersed molten salt systems for methane dehydrogenation, facilitating its path toward commercial viability.

2. Computational methods

Ab initio molecular dynamics simulations are performed using the CPMD code, version 4.3.[45,46] The CPMD code utilizes the Car–Parrinello scheme[47] to perform AIMD simulations. The plane-wave pseudopotential implementation of Kohn–Sham density functional theory was used for the first-principles calculations.[48] The Troullier–Martins pseudopotential[49] with the Perdew–Burke–Ernzerhof generalized gradient approximation[50] was used. The contribution of the non-local part of the pseudopotential to the energy was calculated using the Kleinman–Bylander scheme.[51] In the reciprocal space, integration over the Brillouin zone was performed using only the Γ-point. An energy cutoff of 80 Ryd was optimal to achieve convergence in energy. The Nosé–Hoover

chain[52] thermostat was used to control the electronic and ionic temperatures. The frequency of the ionic thermostat was 3500 cm^{-1}. To avoid coupling between the electronic and ionic dynamics, the frequency of the electron thermostat was chosen 10 000 cm^{-1}. All simulations are performed at 1200 K. In our CPMD simulation, the fictitious electron mass parameter was set to 200 a.u. Short molecular dynamics simulations were performed without the thermostat to estimate an approximate value around which the fictitious electronic kinetic energy fluctuates, and based on these findings, a value of fictitious electronic kinetic energy was selected for subsequent simulations. The time interval for a single step in the molecular dynamics simulation was chosen to be 0.0964 femtoseconds. Initially, geometry optimization was performed to ensure that the energy of the system reached a local minimum. To make sure that the system did not stray off the Born–Oppenheimer surface during the molecular dynamics (MD) simulation, energies, including the fictitious electronic kinetic energy, were monitored. The VMD code was used to visualize AIMD trajectories.[53] The simulation cell size was $10 \times 10 \times 40$ $Å^3$ and the system consists of a four-layered metal catalyst surface with salt molecules positioned on top of the metal layer. This simulation cell replicates the interface between solid metal and liquid molten salt. The modeling of Ni, B-doped Ni, Cu, and B-doped Cu surfaces involved the consideration of their most thermodynamically stable (111) facets using a 4-layer, p(4 × 4) unit cell (*cf.* Fig. 1). Notably, X-ray diffraction (XRD) analysis indicated that both Ni and Cu catalysts exhibits its most intense diffraction peak on the (111) crystallographic plane.[54,55] On the NiB and CuB surfaces, boron atoms occupy the first subsurface octahedral sites within the Ni and Cu slab respectively.[56,57] The significant interaction between neighboring boron atoms results in the reconstruction of the Ni and Cu surface atoms, causing the surface to adopt a stepped appearance. Furthermore, the stability of boron in NiB catalysts can be attributed to a strong bonding interaction between boron 2p orbitals and the Ni 3d band, where the bonding orbitals of octahedral boron shift to −4.8 eV, in contrast to −2.8 eV for boron positioned at the on-surface hcp hollow site.[57] Similarly, it has been shown that at boron doping near 1 monolayer (ML), the subsurface boron layer configuration is the most thermodynamically stable arrangement for the CuB catalyst.[56] To add the salt molecules above the slab, an inter-slab distance of 35 Å was added in the *z*-direction. NaBr molecules were added on the top surface of the metal slab. The number of NaBr molecules added to the box was chosen based on the density of the salt.[32]

CPMD simulations are computationally very expensive, making them impractical to run for the timescales typically required for reactive events to be observed. Therefore, in this current work, the metadynamics method was used as an enhanced sampling technique. The metadynamics algorithm, coupled with CPMD, accelerates the reaction dynamics along selected reaction coordinates and also facilitates the computation of the system's free energy landscape as a function of those coordinates.[58,59] Metadynamics can generate a multidimensional free energy landscape along selected reaction coordinates, providing quantitative information

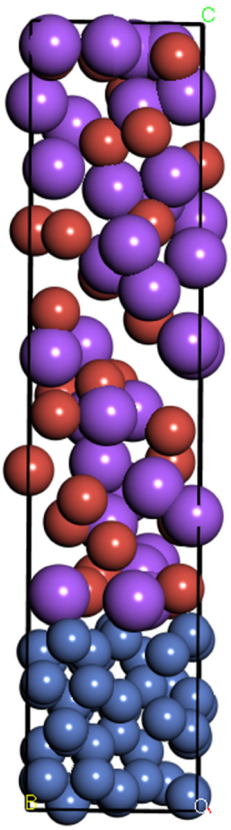

Fig. 1 Representative simulation snapshot of the Ni–NaBr system (one of the four systems studied). The blue balls represent Ni atoms, the red balls represent Br atoms, the violet balls represent Na atoms.

on the energy surface, minimum energy pathways, and barriers. This method, as described by Laio and Gervasio,[60] is based on iteratively "filling up" the free energy landscape of the system by depositing history-dependent potentials at small time intervals in the coordinate space of interest. The accumulation of bias potentials along the metadynamics simulation allows the system to overcome reaction barriers, and it also facilitates the computation of the system's free energy landscape as a function of the specified collective variables (CVs). The height of the bias potential (Gaussian potential) added was maintained at a constant value of 2.6 kJ mol^{-1}. Similar to the original Car–Parrinello approach, the motion of collective variables was decoupled from the motion of ions and fictitious electronic degrees of freedom by selecting a suitable value for the fictitious mass associated with the collective variables. The temperature of the collective variables is maintained at 1200 K, which is the same as the system's physical temperature and is controlled within a range of ±200 K through velocity rescaling. The free energy barriers of sequential dehydrogenation reactions and C–C coupling reactions are computed using metadynamics employing two CVs. A detailed description of CVs that are used for performing metadynamics simulations is presented in Table 1, along with indices of atoms that form the CVs. The convergence of metadynamics simulations is also examined by converging the computed free energy barriers with respect to CPMD-metadynamics steps.

Table 1 Detailed description of CVs and their associated values in the reactant and product state. For clear visualization, NaBr salt above the metal atoms is omitted. The blue balls represent Ni atoms, the white balls represent H atoms, and the gray balls represent C atoms. The atom index is added in the figure

Reaction: $CH_4 \rightarrow CH_3^* + H^*$

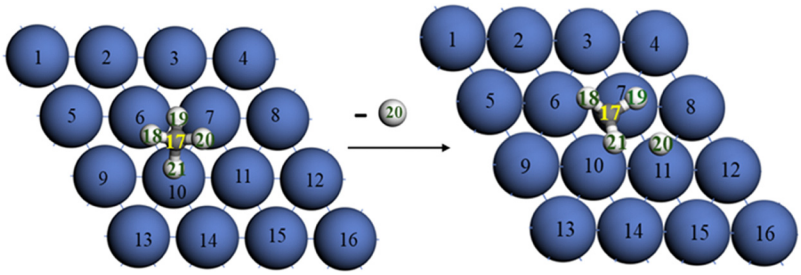

CV	Reactant state	Product state
CV1	0	1
CV2	4	2

CV1: carbon (index 17) and 3 surface metal atoms (indices 6, 7, 10) coordination number
CV2: difference between the coordination number of the C atom (index 17) and one metal atom (index 11) with respect to four hydrogen atoms (indices 18, 19, 20, 21)

Reaction: $CH_3^* \rightarrow CH_2^* + H^*$, $CH_2^* \rightarrow CH^* + H^*$, $CH^* \rightarrow C^* + H^*$

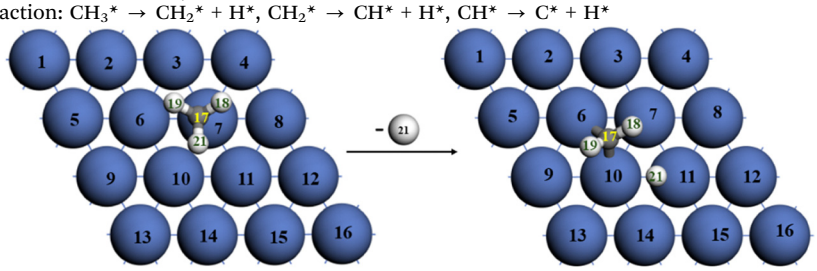

CV	Reactant state	Product state
CV1	3	2
CV2	0	1

CV1: coordination number between C (index 17) and all three H atoms (indices 18, 19, 21)
CV2: coordination number between H (index 21) and 16 surface metal atoms (indices 1–16)

Reaction: $CH_2^* + CH_2^* \rightarrow C_2H_4^*$ and $CH^* + CH^* \rightarrow C_2H_2^*$

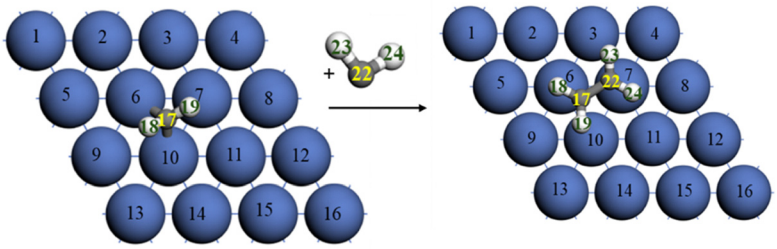

CV	Reactant state	Product state
CV1	−1	0
CV2	−1	0

CV1: difference between the coordination number of one C atom (index 22) and one metal atom (index 6) with respect to another C atom (index 17)
CV2: difference between the coordination number of one C atom (index 17) and one metal atom (index 7) with respect to another C atom (index 22)

For the first dehydrogenation reaction, CH_4 to CH_3^* (where * represents metal surface), one collective variable (CV1) is the coordination number between C (atom index 17) and three surface metal atoms (atom indices 6, 7, 10), and another collective variable (CV2) is the difference between the coordination number of C atom (atom index 17) and one metal atom (atom index 11) with respect to four hydrogen atoms (atom indices 18, 19, 20, 21). CV1 accounts for the interaction of carbon with surface metal atoms, while CV2 characterizes the cleavage of the C–H bond and the formation of the metal–H bond. Before the dehydrogenation of CH_4, values of CV1 and CV2 are 0 and 4, respectively. After the dehydrogenation of CH_4 to CH_3^* and H, these values change to 1 and 2, respectively. In the subsequent dehydrogenation of CH_x (x = 3, 2, 1) to carbon, two key CVs are used. The CV1 is the coordination number between carbon and its hydrogen atoms (atom indices 18, 19, 21), capturing the breaking of C–H bonds during the reaction. The CV2 is the coordination number between the cleaving hydrogen atom and 16 surface metal atoms. For example, in the case of the CH_3^* dehydrogenation reaction the value of CV1 will be 3 before dehydrogenation and will change to 2 after the dehydrogenation. Also, the value of CV2 will change from 0 to 1 before and after the dehydrogenation, respectively. For C–C coupling reactions, CVs include the difference in the coordination number of a carbon atom with respect to another carbon and the metal atom to which it is attached. This way, we can take into account the formation of the C–C bond and also the dissociation of the metal–C bond (*cf.* Table 1).

3. Results and discussion

In the current study, we investigated the sequential catalytic dehydrogenation of CH_4 to carbon, involving intermediate

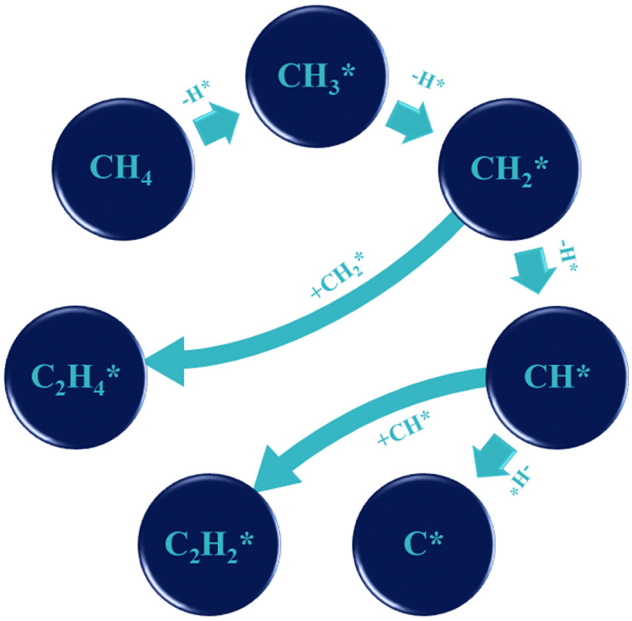

Fig. 2 Reaction network of CH_4 sequential dehydrogenation and C–C couplings (CH_2–CH_2 and CH–CH) routes that are investigated in this work.

species CH_3*, CH_2*, and CH* (*cf.* Fig. 2). Simultaneously, we examined the coupling reactions of CH_2* and CH* species, to produce ethylene and acetylene, respectively, as shown in the reaction scheme in Fig. 2. These reactions were investigated in Ni, NiB, Cu, and CuB dispersed molten salt systems, and the results are presented in the following sections.

3.1 Dehydrogenation of CH_4 to CH_3

The rate-limiting step in the sequential dehydrogenation of methane is usually its first activation, which involves the breaking of the strong C–H bond.[61,62] The free energy surfaces computed using CPMD-metadynamics for the dehydrogenation of CH_4 to CH_3*, as a function of the collective variables defined in Table 1, are shown in Fig. 3(a)–(d) for Ni–NaBr, NiB–NaBr, Cu–NaBr, and CuB–NaBr respectively. The free energy barrier for the dehydrogenation of CH_4 to CH_3* in the Ni–NaBr system is 151 kJ mol^{-1}. The effective activation energy for methane pyrolysis in a differential bubble column reactor using pure molten NaBr salt was reported to be 295 kJ mol^{-1},[32] which is significantly higher than the free energy barrier of CH_4 dehydrogenation in the Ni–NaBr system. The presence of Ni in NaBr leads to a reduction in the free energy barrier due to the back-donation from the Ni 3d orbitals to the antibonding σ_{CH^*} orbital in methane. In the case of the NiB–NaBr system, the free energy barrier for the first dehydrogenation of methane is further reduced to 112 kJ mol^{-1}. It shows that the boron doping in the first subsurface layer of Ni has a significant effect on the C–H activation of methane. The reduction in the activation barrier can be ascribed to the formation of a steplike surface reconstruction, which arises from the attractive interaction among boron atoms located in adjacent octahedral sites. Moreover, the doping of B in the subsurface Ni causes charge transfer from Ni to B, which in turn increases the catalytic activity of NiB for CH_4 dehydrogenation.[57] Xu *et al.*'s DFT calculations indicated that the surface reconstruction of NiB lowers the methane activation barrier by 27 kJ mol^{-1}.[57] Mohan *et al.* also reported that the free energy barriers at 973 K for the first methane activation for Ni and NiB catalysts, as determined by gas phase DFT calculations, were 164 kJ mol^{-1} and 107 kJ mol^{-1}, respectively.[63] The gas phase free energy barriers for C–H activation on Ni and NiB closely match our calculation. Hence, it can be inferred that NaBr (and its interface with the catalyst surface) has very little effect on C–H activation. Interestingly, in the Cu–NaBr system, the free energy barrier for CH_4 dehydrogenation to CH_3* is 91 kJ mol^{-1}, which is significantly lower than the Ni-based systems. Copper is a relatively weaker catalyst for C–H activation due to its filled d-orbital. It is reported in the literature that the first CH_4 dehydrogenation barrier in the gas phase on the Cu(111) surface is 174 kJ mol^{-1}.[56] In our case, the reduction in the dehydrogenation barrier of CH_4 to CH_3* can be attributed to the distortion of the Cu surface at this high temperature (which is captured in the finite temperature CPMD simulations, unlike ground-state DFT simulations), making it much more catalytically active than the planar Cu surface. Our simulation study at 1200 K demonstrated that the finite temperature effect on the Cu structure is significantly more pronounced than on the Ni structure. This can be attributed to the fact that Cu has a melting point of 400 °C lower than Ni. Therefore, at high temperatures, Cu exhibits higher catalytic activity due to the agglomeration of Cu atoms. Varghese *et al.* also reported a comparable free energy barrier of 90 kJ mol^{-1} at 1273 K for methane dissociation on the Cu_6 cluster.[64] Varghese *et al.* noted that the collision-induced vibrational activation of stretching and bending modes, coupled with lattice relaxation of the clusters, significantly lowers the free energy barrier for methane dissociation on Cu clusters.[64] They also discovered that increasing the cluster size provides a greater number of sites for the chemisorption of the dissociated fragments (CH_3 and H), thus reducing the free energy barrier for methane dissociation.[64] Hence, the Cu catalyst would increase the catalytic activity of the weak NaBr salt for the non-oxidative dehydrogenation of methane. In the case of the CuB–NaBr system, the dehydrogenation barrier (86 kJ mol^{-1}) is further reduced by 5 kJ mol^{-1} in comparison with the Cu–NaBr system. Similar to that of Ni, doping of B into the first subsurface layer of Cu causes the formation of the stepped surface at the top due to the B–B interaction, which generates active sites that effectively activate methane C–H bonds. Thang *et al.* reported that, in addition to surface reconstructions, incorporating a monolayer of sub-surface boron into the copper lattice induces charge transfer from boron to copper, which subsequently enhances the activity for methane C–H bond cleavage.[56] The value of the free energy barrier is consistent with the gas phase activation barrier (75 kJ mol^{-1}) for methane dehydrogenation reported by Thang *et al.*[56] Hence, doping of B into the subsurface layer of Cu also acts as a promoter for the C–H activation of methane.

In brief, our CPMD simulation study revealed that the doping of B in both Ni and Cu catalysts enhanced its catalyst activity, whereas the temperature-induced microstructural

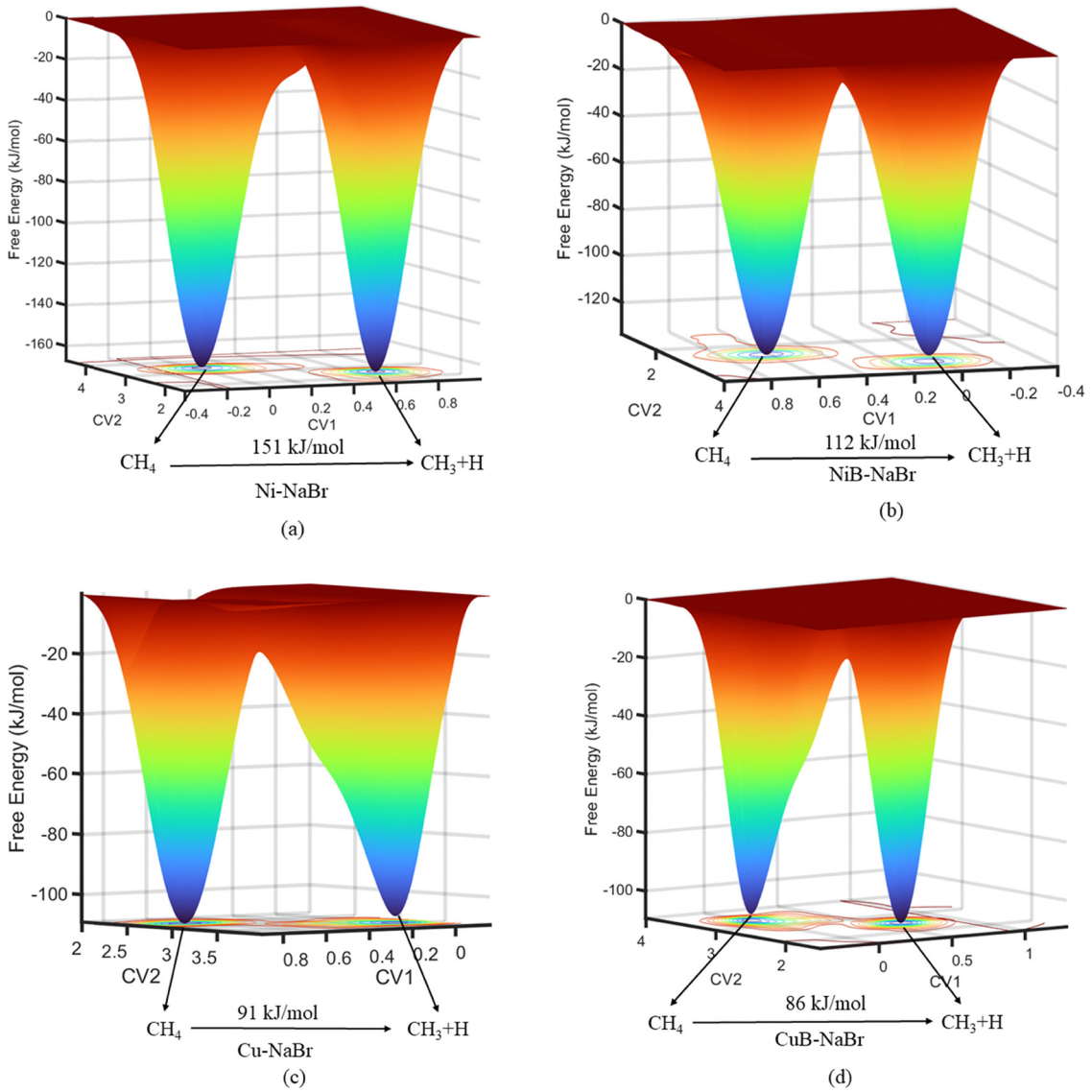

Fig. 3 The free energy surface reconstructed at 1200 K from CPMD-metadynamics simulations for the CH_4 dehydrogenation to CH_3 in (a) Ni–NaBr, (b) NiB–NaBr, (c) Cu–NaBr, and (d) CuB–NaBr metal-molten media systems. The free energy barrier in kJ mol^{-1} is shown above the arrow. Refer to Table 1 for the definition of collective variables CV1 and CV2.

change in Cu is responsible for the reduction of the first methane dehydrogenation barrier on it. It is also observed that the presence of molten NaBr at the interface did not significantly affect the methane dehydrogenation barrier.

3.2 Sequential dehydrogenation of CH_x (x = 3, 2, 1) and C–C coupling

Free energy barriers for the sequential dehydrogenation of CH_x (x = 3, 2, 1) and the coupling of CH_2* and CH* species in all four metal dispersed systems are provided in Fig. 4. The free energy surfaces for the sequential dehydrogenation of CH_x (x = 3, 2, 1) to C are given in Fig. S1–S3 (ESI†). Free energy profiles for the CH_2–CH_2 coupling reaction in all four systems are shown in Fig. 5; whereas free energy profiles for the CH–CH coupling are given in Fig. S4 (ESI†). We did not simulate CH_3* coupling because significant steric hindrance prevents CH_3* fragments from coupling. The sp^3 carbon's tetrahedral geometry leads to a weak catalyst-reactant interaction, resulting in a very high free energy barrier for coupling. Notably, the free energy barrier for CH_3–CH_3 coupling on a CuB catalyst is 273 kJ mol^{-1}, as determined from gas phase calculations.[56]

In the Ni–NaBr system, the free energy barrier for the formation of CH_2* is 54 kJ mol^{-1}, and the formation of CH* is 50 kJ mol^{-1}. However, the formation of carbon from the CH* intermediate requires overcoming a barrier of 88 kJ mol^{-1}, which is significantly higher than the previous dehydrogenation steps. The first dehydrogenation barrier (151 kJ mol^{-1}) of CH_4 is also much higher than the free energy barriers of subsequent dissociation steps in the Ni–NaBr system. Mohan *et al.* reported free energy barriers (using DFT calculations) at 973 K and 10 bar pressure for the dehydrogenation of CH_3*, CH_2*, and CH* on the Ni(111) surface as 164 kJ mol^{-1},

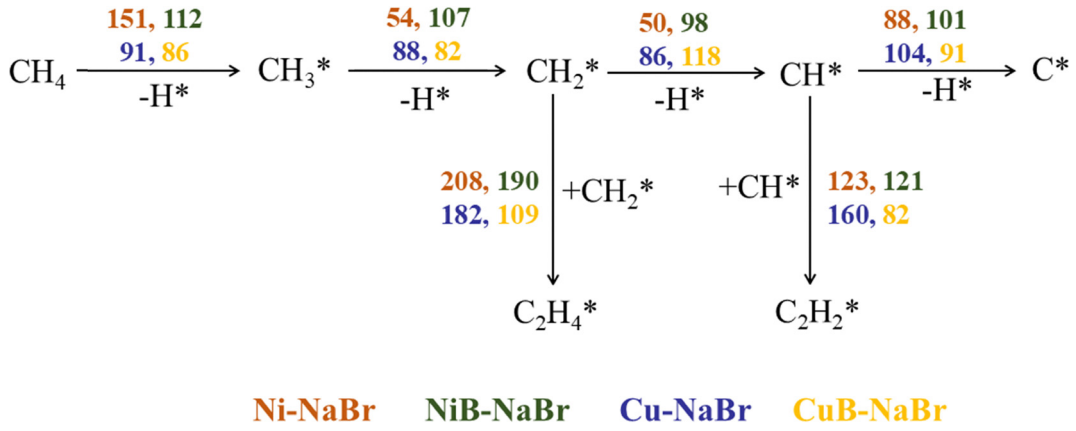

Fig. 4 Metadynamics calculated free energy barriers (kJ mol^{-1}) at 1200 K of all elementary reactions for sequential dehydrogenation of methane and C–C coupling reaction on Ni–NaBr, NiB–NaBr, Cu–NaBr, CuB–NaBr system. Red, green, blue, and yellow colors represent Ni–NaBr, NiB–NaBr, Cu–NaBr, and CuB–NaBr systems respectively.

58 kJ mol^{-1}, 35 kJ mol^{-1}, and 126 kJ mol^{-1} respectively.[63] Interestingly, our calculated free energy barrier of CH_2–CH_2 coupling is 208 kJ mol^{-1} which is significantly higher than the dehydrogenation barrier (50 kJ mol^{-1}) of CH_2* to CH*. So, the coupling reaction is kinetically unfavorable in the Ni–NaBr system. As a result, the Ni–NaBr system will follow the dehydrogenation pathway of CH_2* over its coupling. It is also found that the free energy barrier of the CH–CH coupling is 123 kJ mol^{-1}, which is 35 kJ mol^{-1} more than the dissociation barrier of the CH* intermediate. So, the CH* dehydrogenation reaction is also kinetically more favorable than the CH–CH coupling reaction. Hence, we predict that in the Ni–NaBr system, methane would undergo complete dehydrogenation to produce hydrogen and carbon.

For the NiB–NaBr system, the calculated free energy barrier for CH_3* dehydrogenation to CH_2* is 102 kJ mol^{-1}. The barrier for CH_2* conversion to CH* is 98 kJ mol^{-1}, while the dissociation of CH* to C* has a barrier of 101 kJ mol^{-1}. In the NiB–NaBr system, the dehydrogenation barriers for CH_3* and CH_2* species are slightly higher compared to those in the Ni–NaBr medium. The literature reports that the calculated free energy barriers (using ground-state DFT) at 973 K for the dehydrogenation of CH_3*, CH_2*, and CH* on the NiB surface are 87 kJ mol^{-1}, 56 kJ mol^{-1}, and 96 kJ mol^{-1}, respectively,[63] indicating that our calculated free energy barriers for sequential dehydrogenation in the NiB–NaBr system are consistent with these DFT-calculated values on the NiB surface. The computed free energy barrier of CH_2–CH_2 coupling in the NiB–NaBr molten media is 190 kJ mol^{-1}. However, this coupling barrier is significantly higher than the free energy barrier (98 kJ mol^{-1}) of the CH_2* dehydrogenation. Similarly, the CH–CH coupling reaction in the NiB–NaBr system must overcome an energy barrier of 121 kJ mol^{-1}, which is higher than the free energy barrier for CH* dehydrogenation. Therefore, the NiB–NaBr system is also kinetically less favorable for the formation of C_2H_4 and C_2H_2 than the complete dehydrogenation of CH_4.

For the Cu–NaBr system, the free energy barrier for the dehydrogenation of CH_3* to CH_2* is 88 kJ mol^{-1}. Additionally, the free energy barriers for the formation of CH* species from CH_2* and the dehydrogenation of CH* to C* are 86 kJ mol^{-1} and 104 kJ mol^{-1}, respectively. Furthermore, it is observed that the free energy barrier for CH* dissociation to C* is the highest among all dehydrogenation steps of CH_4. This aligns with previous findings, indicating that the formation of carbon exhibits the highest barrier among the elementary dehydrogenation steps on the Cu(111) surface.[65–67] Moreover, the calculated free energy barrier (*cf.* Fig. 4) for the CH_2–CH_2 coupling reaction in the Cu–NaBr system is 182 kJ mol^{-1}, which is 96 kJ mol^{-1} higher than the dehydrogenation barrier of CH_2* to CH*. Therefore, the Cu–NaBr system does not kinetically favor the CH_2–CH_2 coupling reaction over the dehydrogenation of CH_2* to CH*. Similarly, the CH–CH coupling barrier in this molten medium is 160 kJ mol^{-1}, which is higher than the dehydrogenation barrier of CH* to C*. Therefore, the Cu–NaBr system is more likely to favor the dehydrogenation of CH* to C* over the coupling reaction. Therefore, the Cu–NaBr molten medium favors the complete dehydrogenation of CH_4 over C–C coupling.

In the CuB–NaBr system, the C–H activation barrier of the CH_3* fragment is 82 kJ mol^{-1}, which is about the same as the methane dehydrogenation barrier. The subsequent dehydrogenation barriers of CH_2* and CH* species are 118 kJ mol^{-1} and 91 kJ mol^{-1} respectively. In the CuB–NaBr system, the dehydrogenation of CH_2* presents the highest energy barrier compared to other dehydrogenation steps. Interestingly, in the case of CuB, the free energy barrier for the coupling of the CH_2* fragment (109 kJ mol^{-1}) is lower than that for the CH_2* dehydrogenation barrier (118 kJ mol^{-1}). Accordingly, the CuB–NaBr system would kinetically promote the CH_2–CH_2 coupling reaction over the CH_2* dehydrogenation. This free energy barrier for the coupling of CH_2* species, in the presence of the molten media, is consistent with the activation barrier (120 kJ mol^{-1}) of CH_2–CH_2 coupling on the CuB catalyst in the gas phase.[56] It was reported that the coupling of CH_2* fragments on CuB was more favorable due to the strong binding of ethylene in the π-configuration at the step sites of the Cu in CuB.[56] Additionally, Sargent and coworkers have experimentally studied the electrochemical reduction of CO_2 (CO2RR) to C_2 hydrocarbons on the CuB catalyst.[68] They have observed that

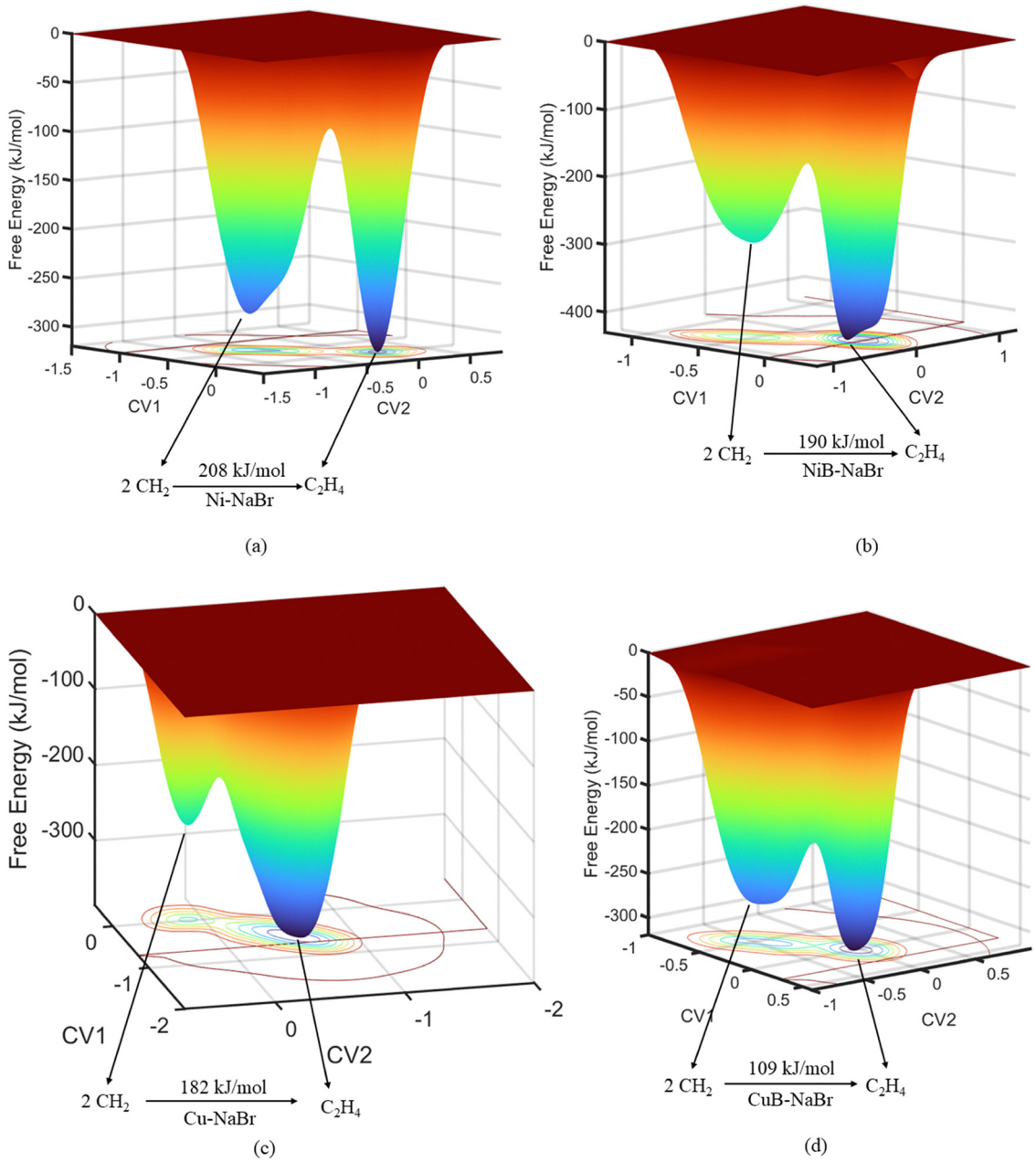

Fig. 5 Metadynamics calculated free energy reaction profile at 1200 K for the CH_2–CH_2 coupling (a) Ni–NaBr, (b) NiB–NaBr, (c) Cu–NaBr, and (d) CuB–NaBr are shown. The free energy barrier (kJ mol^{-1}) is shown above the arrow. Refer to Table 1 for the definition of collective variables CV1 and CV2.

the doping of B in Cu gave highly selective C_2 products from CO_2 by facilitating C–C coupling.[68] Nie *et al.* studied C–C coupling on Fe–Cu bimetallic catalyst in CO_2 hydrogenation.[69] They have reported, using DFT calculations, that the addition of Cu in Fe(100) reduced the activation barrier of CH_2–CH_2 and CH–CH coupling by 40 kJ mol^{-1} and 45 kJ mol^{-1}, respectively in comparison with pristine Fe(100) surface.[69] Our calculated free energy barrier shows that the CH–CH coupling barrier (82 kJ mol^{-1}) for the CuB–NaBr molten medium is slightly lower than the dehydrogenation barrier (91 kJ mol^{-1}) of CH*. Hence, we predict that the CuB–NaBr molten system would kinetically favor CH_2*–CH_2* and CH*–CH* coupling over complete dehydrogenation to C.

In summary, we observed that, except for the CuB–NaBr molten salt system, the sequential dehydrogenation barrier of CH_4 is lower than that of the C–C coupling reactions in all metal–metal salt systems. This suggests that the Ni, NiB, and Cu-dispersed molten salt systems would kinetically favor the complete dehydrogenation of CH_4 over non-oxidative coupling at 1200 K. Interestingly, it is observed that in the CuB–NaBr system, the barriers for CH_2–CH_2 and CH–CH coupling are lower than those for the dehydrogenation steps of CH_2* and CH*. Hence, the CuB–NaBr system would kinetically promote both CH_2–CH_2 and CH–CH coupling reactions, making the CuB–NaBr molten medium a promising candidate for producing C_2 products and

hydrogen *via* non-oxidative coupling of methane. Moreover, the presence of molten salt does not adversely impact the catalyst's activity; in fact, it enhances heat transfer within the molten medium and aids in the removal of solid carbon from the molten medium.

3.3 Carbon diffusion and catalyst stability

Carbon produced as a by-product during the sequential dehydrogenation of methane can be deposited on the active sites of the metal and can diffuse into the bulk, deactivating the catalyst. Hence, we investigated carbon diffusion into the four active metals by positioning carbon at the interface between the molten salt and the metal. We performed the CPMD simulations at 1200 K for more than 8 picoseconds (ps) to check the migration of the carbon into the metals. In these simulations, no bias potential was applied to the system, and the dynamics of carbon within each catalyst at different time steps are depicted in Table 2. It is emphasized that the carbon diffusion in the catalyst can be observed through AIMD simulations, but not through ground-state DFT calculations. Our simulations show that within the first 4 ps, even without implementing any enhanced sampling method, carbon diffuses from the top of the Ni surface to the subsurface region. This suggests that Ni would suffer from deactivation due to the diffusion of carbon into Ni bulk (*cf.* Table 2). Additionally, we calculated the distance between the carbon atom and the surface Ni atoms. The distance between the carbon atom and the surface Ni atoms along the CPMD trajectory is shown in Fig. 6a. We found that the carbon atom on the top surface ($\sim$1.5 Å) diffuses into the subsurface layer of the Ni catalyst after 2 ps. Our results are in excellent agreement with coke deposition studies on Ni catalysts. For example, Xu *et al.* observed that on the terraces of a Ni catalyst, the carbon atoms are not very stable.[57] They noted that these atoms preferably diffuse to subsurface octahedral sites and step sites, as it is thermodynamically more favorable.[57] Tarazkar *et al.* also studied carbon diffusion in a

Table 2 Time evolution of carbon in the four molten mediums. The highlighted yellow circle in the image represents the position of the carbon atom. The blue balls represent Ni atoms, the white balls represent H atoms, the peach balls represent Cu atoms, the salmon balls represent B atoms, and the gray ball represents a C atom. For clear visualization, a portion of the slab containing a few salt and metal atoms is shown

	Time steps		
Molten medium	0 ps	4 ps	8 ps
Ni–NaBr	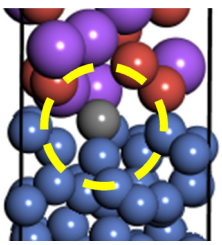	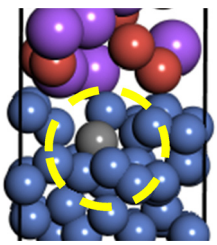	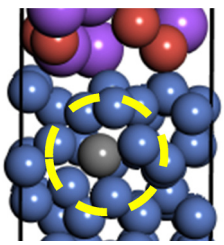
NiB–NaBr	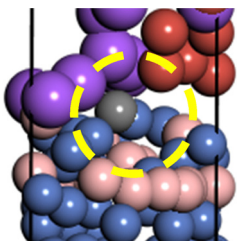	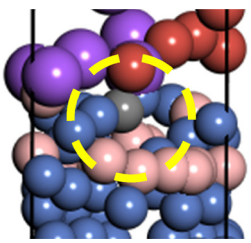	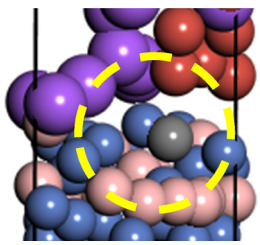
Cu–NaBr	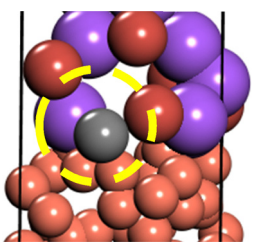	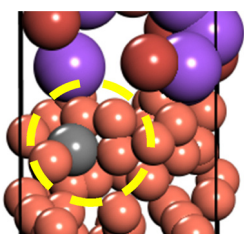	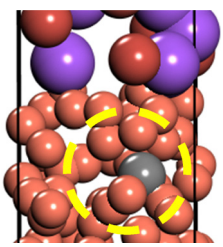
CuB–NaBr	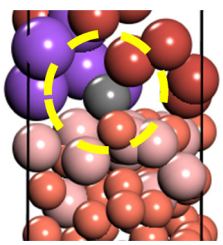	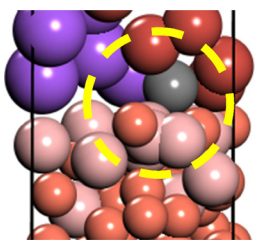	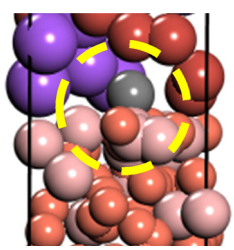

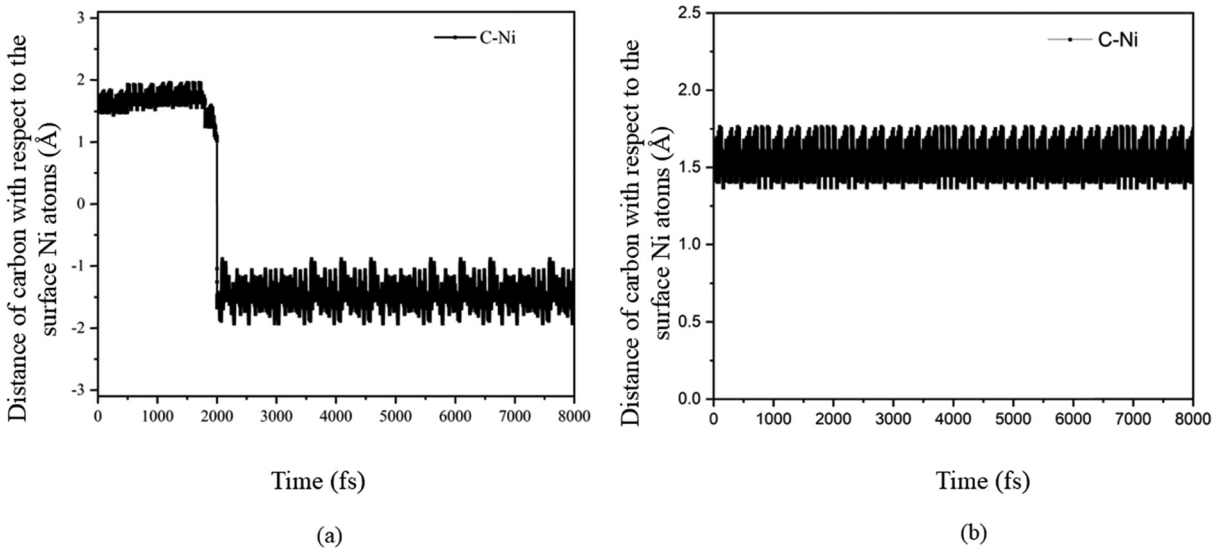

Fig. 6 Time trajectory of the distance between the carbon atom and the surface Ni atoms during CPMD simulation for (a) Ni–NaBr and (b) NiB–NaBr system.

molten NaBr–Ni(111) system.[37] They also found that carbon rapidly migrates from the interface NaBr–Ni(111) interface to the subsurface of Ni. Experimental observation revealed the formation of a bulk nickel carbide due to the methane dissociation on Ni(110) and Ni(100) surfaces at temperatures above 533 K.[70] Therefore, it is necessary to inhibit carbon diffusion into the metal to prevent catalyst deactivation. In the case of the NiB–NaBr system, we have observed that carbon is unable to diffuse into the NiB catalyst and resides on the top surface of the NiB catalyst. Furthermore, the limited variation in the distance of the carbon atom relative to the top Ni layer (*cf.* Fig. 6b) also indicates that the carbon atom does not migrate from the top of the surface to the subsurface layers of the NiB catalyst. This occurs due to the selective blocking of subsurface, interstitial sites in Ni by boron. It has also been reported that the boron promoter in the first subsurface layer lowers the carbon binding energy on the surface, potentially reducing carbon coverage.[71] Hence, doping of B effectively prevents the diffusion of carbon into the Ni particle. Xu *et al.* also found that doping the subsurface of nickel catalysts with boron prevents carbon diffusion into the Ni catalyst.[57,71] Our study demonstrates that even at an elevated temperature of 1200 K the NiB–NaBr system remains stable and does not experience any carbon diffusion into the bulk, ensuring that its catalytic activity remains unaffected, and thus nickel carbide would not form. Similar to the Ni–NaBr system, we have also observed carbon diffusion occurring in the Cu–NaBr system and carbon migrates into the bulk of Cu. Similar to the Ni–NaBr system, the variation in the distance of the C atom from the top Cu layer (*cf.* Fig. S6a, ESI†) further demonstrates its migration from the top surface into the bulk Cu. Therefore, coke deposition on its active site would lead to a reduction in the catalytic activity of the Cu–NaBr system. Typically, the formation of C* species from CH_3* species is not observed on catalytically weak Cu catalysts.[65,67] However, we investigated the complete dehydrogenation of methane to carbon at a very high temperature (1200 K). As the Cu structure gets distorted at high temperatures, it contains more void spaces than the flat Cu surface (usually employed in ground-state DFT simulations). Hence, we observed that carbon diffuses through the distorted Cu surface into the bulk. Zeng *et al.* also observed carbon deposition during methane dehydrogenation on the Cu(111) surface at 1300 K temperature.[62] Remarkably, there is no carbon diffusion into the catalyst observed for the CuB–NaBr system. Similar to the NiB–NaBr system, it has been observed in the CuB–NaBr molten medium that doping B into the first subsurface layer of Cu prevents carbon migration from the top surface into the bulk of the catalyst, even at high temperatures. Additionally, the variation in the distance (*cf.* Fig. S6b, ESI†) of the carbon atom relative to the top Cu layer further elucidates that carbon does not diffuse into the subsurface layers of the CuB catalyst. Therefore, the doping of B in both the NiB–NaBr and CuB–NaBr systems serves to inhibit coke deposition. Additionally, we did not observe any leaching of metal atoms from the catalyst into the molten salt and the diffusion of boron from the subsurface to the on-surface at such elevated temperatures. Since our simulations consider finite temperature effects and dynamics, unlike conventional DFT, this further proves the stability of boron-doped catalysts.

4. Conclusions

We investigated the sequential dehydrogenation and non-oxidative coupling of methane in solid metal-dispersed molten salt systems using *ab initio* molecular dynamics simulations with the Car–Parrinello scheme. In this study, activity, selectivity, and stability of four metal catalysts, namely Ni, Cu, and boron-doped Ni and Cu catalysts, in molten NaBr salt were investigated under *operando* conditions at 1200 K. It was found that the presence of a heterogeneous catalyst enhances the catalytic activity of the molten media significantly (methane

activation barrier is 151 kJ mol^{-1} for the Ni–NaBr medium). The doping of B in the Ni catalyst further increased the catalytic activity by lowering the first CH_4 activation barrier (112 kJ mol^{-1}). Structural changes in the Cu catalyst at 1200 K, in the presence of molten media, are more pronounced than in the Ni catalyst. Due to temperature-induced distortions in the molten salt, the catalytic activity of the Cu–NaBr system significantly increased, which, in turn, significantly lowered the barrier for methane dehydrogenation (91 kJ mol^{-1}) as compared to that on a flat Cu(111) surface. Incorporating a monolayer of sub-surface boron also induces slight reconstruction of the copper surface, resulting in a further reduced energy barrier for the first methane dehydrogenation (86 kJ mol^{-1}). Additionally, it was observed that the free energy barriers for CH_x (x = 1, 2) coupling reactions are higher than those for the sequential dehydrogenation of CH_4 in the Ni, NiB, and Cu-dispersed molten salt systems. Interestingly, the free energy barriers for C–C coupling reactions are lower than the dehydrogenation barriers in the CuB–NaBr medium, indicating that this metal-dispersed molten salt will kinetically promote the formation of valuable C_2 products carbon. Furthermore, the diffusion of carbon into the bulk catalyst was observed at elevated temperatures for pure Ni and Cu catalysts, while the doping of B in the first subsurface layer of Ni and Cu prevents its diffusion into the bulk. Additionally, no leaching of metal atoms from the catalyst into the metal salt medium and no migration of the boron from the sub-surface to the on-surface at such elevated temperatures. Thus, boron doping in the catalyst not only enhanced the catalytic activity but also improved the stability of the catalysts by preventing carbon diffusion into the bulk and promoting C–C coupling reactions in the case of CuB. Based on this condensed phase, finite temperature dynamic simulation study, which resembles the experimental conditions much closer than usual DFT, we conclude that the NiB–NaBr system is well-suited for hydrogen and carbon production, while the CuB–NaBr system shows potential as a molten medium for generating H_2 and valuable C_2 products from methane. The mechanistic insights of this work will facilitate the development of active and stable metal-dispersed molten salt systems for CO_2-free hydrogen generation from natural gas.

Author contributions

Pritam Rudra: writing – original draft, writing – review & editing, visualization, validation, software, methodology, investigation, formal analysis, data curation, conceptualization. Ojus Mohan: writing – review & editing, visualization, validation, supervision, software, resources, project administration, methodology, investigation, funding acquisition, data curation, conceptualization. Samir H. Mushrif: writing – review & editing, supervision, resources, project administration, funding acquisition, conceptualization.

Data availability

The data supporting this article have been included as part of the ESI.†

Conflicts of interest

The authors declare no competing financial interest.

Acknowledgements

S. H. M. acknowledges the financial support by NSERC Canada and the Faculty of Engineering at the University of Alberta and the computational resources provided by the Digital Research Alliance of Canada. O. M. acknowledges the new faculty seed grant from IIT Bombay: RD/0522-IRCCSH0-012 and the computational support provided by the Spacetime HPC facility at IIT Bombay and the National Supercomputing Mission (NSM) for providing computing resources on 'PARAM Siddhi-AI'.

References

1 M. J. Economides and D. A. Wood, The state of natural gas, *J. Nat. Gas Sci. Eng.*, 2009, **1**, 1–13.
2 E. McFarland, Unconventional chemistry for unconventional natural gas, *Science*, 2012, **338**, 341–342.
3 A. Bakenne, W. Nuttall and N. Kazantzis, Sankey-Diagram-based insights into the hydrogen economy of today, *Int. J. Hydrogen Energy*, 2016, **41**, 7744–7753.
4 S. Dürr, *et al.*, Carbon Dioxide-Free Hydrogen Production with Integrated Hydrogen Separation and Storage, *ChemSusChem*, 2017, **10**, 42–47.
5 A. Holmen, O. Olsvik and O. A. Rokstad, Pyrolysis of natural gas: chemistry and process concepts, *Fuel Process. Technol.*, 1995, **42**, 249–267.
6 H. Schwarz, Chemistry with methane: Concepts rather than recipes, *Angew. Chem., Int. Ed.*, 2011, **50**, 10096–10115.
7 S. Abanades and G. Flamant, Thermochemical hydrogen production from a two-step solar-driven water-splitting cycle based on cerium oxides, *Sol. Energy*, 2006, **80**, 1611–1623.
8 F. Billaud, C. Gueret and J. Weill, Thermal decomposition of pure methane at 1263 K. Experiments and mechanistic modelling, *Thermochim. Acta*, 1992, **211**, 303–322.
9 X. Guo, *et al.*, Direct, nonoxidative conversion of methane to ethylene, aromatics, and hydrogen, *Science*, 2014, **344**, 616–619.
10 A. D. Talpade, *et al.*, Catalytic reactivity of Pt sites for non-oxidative coupling of methane (NOCM), *Chem. Eng. J.*, 2024, **481**, 148675.
11 T. I. Korányi, M. Németh, A. Beck and A. Horváth, Recent Advances in Methane Pyrolysis: Turquoise Hydrogen with Solid Carbon Production, *Energies*, 2022, **15**, 6342.
12 M. Msheik, S. Rodat and S. Abanades, Methane cracking for hydrogen production: A review of catalytic and molten media pyrolysis, *Energies*, 2021, **14**, 3107.
13 B. Parkinson, P. Balcombe, J. F. Speirs, A. D. Hawkes and K. Hellgardt, Levelized cost of CO2 mitigation from hydrogen production routes, *Energy Environ. Sci.*, 2019, **12**, 19–40.
14 P. Schwach, X. Pan and X. Bao, Direct Conversion of Methane to Value-Added Chemicals over Heterogeneous

Catalysts: Challenges and Prospects, *Chem. Rev.*, 2017, **117**, 8497–8520.
15 J. Bae, *et al.*, Non-oxidative methane conversion by Fe single site catalysts: quantifying temperature limitations imposed by gas-phase pyrolysis, *Catal. Sci. Technol.*, 2022, **12**, 6903–6919.
16 C. Karakaya and R. J. Kee, Progress in the direct catalytic conversion of methane to fuels and chemicals, *Prog. Energy Combust. Sci.*, 2016, **55**, 60–97.
17 Y. Li, D. Li and G. Wang, Methane decomposition to COx-free hydrogen and nano-carbon material on group 8-10 base metal catalysts: A review, *Catal. Today*, 2011, **162**, 1–48.
18 A. M. Amin, E. Croiset and W. Epling, Review of methane catalytic cracking for hydrogen production, *Int. J. Hydrogen Energy*, 2011, **36**, 2904–2935.
19 U. P. M. Ashik, W. M. A. Wan Daud and H. F. Abbas, Production of greenhouse gas free hydrogen by thermocatalytic decomposition of methane – A review, *Renewable Sustainable Energy Rev.*, 2015, **44**, 221–256.
20 M. S. Liao and Q. E. Zhang, Dissociation of methane on different transition metals, *J. Mol. Catal. A: Chem.*, 1998, **136**, 185–194.
21 M. D. Argyle and C. H. Bartholomew, Heterogeneous catalyst deactivation and regeneration: A review, *Catalysts*, 2015, **5**, 145–269.
22 M. McConnachie, M. Konarova and S. Smart, Literature review of the catalytic pyrolysis of methane for hydrogen and carbon production, *Int. J. Hydrogen Energy*, 2023, **48**, 25660–25682.
23 Y. I. Matatov-Meytal, M. Sheintuch, G. E. Shter and G. S. Grader, Optimal temperatures for catalytic regeneration of activated carbon, *Carbon*, 1997, **35**, 1527–1531.
24 E. T. C. Vogt, D. Fu and B. M. Weckhuysen, Carbon Deposit Analysis in Catalyst Deactivation, Regeneration, and Rejuvenation, *Angew. Chem., Int. Ed.*, 2023, **62**, e202300319.
25 I. Wang, *et al.*, Catalytic decomposition of methane into hydrogen and high-value carbons: combined experimental and DFT computational study, *Catal. Sci. Technol.*, 2021, **11**, 4911–4921.
26 P. Xie, *et al.*, Nanoceria-Supported Single-Atom Platinum Catalysts for Direct Methane Conversion, *ACS Catal.*, 2018, **8**, 4044–4048.
27 C. Palmer, *et al.*, Methane Pyrolysis with a Molten Cu–Bi Alloy Catalyst, *ACS Catal.*, 2019, **9**, 8337–8345.
28 D. C. Upham, *et al.*, Catalytic molten metals for the direct conversion of methane to hydrogen and separable carbon, *Science*, 2017, **358**, 917–921.
29 L. Chen, *et al.*, Ternary NiMo-Bi liquid alloy catalyst for efficient hydrogen production from methane pyrolysis, *Science*, 2023, **381**, 857–861.
30 J. Kim, *et al.*, Catalytic methane pyrolysis for simultaneous production of hydrogen and graphitic carbon using a ceramic sparger in a molten NiSn alloy, *Carbon*, 2023, **207**, 1–12.
31 N. Rahimi, *et al.*, Solid carbon production and recovery from high temperature methane pyrolysis in bubble columns containing molten metals and molten salts, *Carbon*, 2019, **151**, 181–191.
32 C. Palmer, M. Tarazkar, M. J. Gordon, H. Metiu and E. W. Mcfarland, Methane pyrolysis in low-cost, alkali-halide molten salts at high temperatures, *Sustainable Energy Fuels*, 2021, **5**, 6107–6123.
33 D. Kang, N. Rahimi, M. J. Gordon, H. Metiu and E. W. McFarland, Catalytic methane pyrolysis in molten MnCl2-KCl, *Appl. Catal., B*, 2019, **254**, 659–666.
34 D. Kang, *et al.*, Catalytic Methane Pyrolysis in Molten Alkali Chloride Salts Containing Iron, *ACS Catal.*, 2020, **10**, 7032–7042.
35 B. Parkinson, C. F. Patzschke, D. Nikolis, S. Raman and K. Hellgardt, Molten salt bubble columns for low-carbon hydrogen from CH4 pyrolysis: Mass transfer and carbon formation mechanisms, *Chem. Eng. J.*, 2021, **417**, 127407.
36 C. F. Patzschke, *et al.*, Co–Mn catalysts for H2 production via methane pyrolysis in molten salts, *Chem. Eng. J.*, 2021, **414**, 128730.
37 M. Tarazkar, H. Metiu and H. H. Kristoffersen, Properties of Methane and Carbon Adsorbed at the Interface between Molten NaBr and Ni(111), *J. Phys. Chem. C*, 2021, **125**, 3980–3987.
38 J. J. Varghese and S. H. Mushrif, Origins of complex solvent effects on chemical reactivity and computational tools to investigate them: A review, *React. Chem. Eng.*, 2019, **4**, 165–206.
39 F. Saiz and L. Bernasconi, Catalytic properties of the ferryl ion in the solid state: a computational review, *Catal. Sci. Technol.*, 2022, **74**, 3069–3087.
40 F. Saiz and L. Bernasconi, Entropic influence on the generation of Fe(iv)O species at mononuclear Fe(ii) sites in metal-organic frameworks, *Catal. Sci. Technol.*, 2023, **13**, 5689–5701.
41 D. J. Vogel, J. M. Rimsza and T. M. Nenoff, Prediction of Reactive Nitrous Acid Formation in Rare-Earth MOFs *via ab initio* Molecular Dynamics, *Angew. Chem., Int. Ed.*, 2021, **60**, 11514–11522.
42 L. Bonati *et al. The role of dynamics in heterogeneous catalysis: Surface diffusivity and N2 decomposition on Fe(111)*, 2023, pp. 1–11, DOI: **10.1073/pnas.2313023120/-/DCSupplemental.Published**.
43 S. K. Dutta, B. Singh, H. Metiu and V. Agarwal *Increase of the Catalytic Activity of Molten Salts by Doping: Methane Activation*, 2023, pp. 1–6, DOI: **10.1021/acs.jpcc.3c07024**.
44 J. Zeng, *et al.*, Catalytic Methane Pyrolysis with Liquid and Vapor Phase Tellurium, *ACS Catal.*, 2020, **10**, 8223–8230.
45 W. Andreoni and A. Curioni, New advances in chemistry and materials science with CPMD and parallel computing, *Parallel Comput.*, 2000, **26**, 819–842.
46 R. Iftimie, P. Minary and M. E. Tuckerman, Ab initio molecular dynamics: Concepts, recent developments, and future trends, *Proc. Natl. Acad. Sci. U. S. A.*, 2005, **102**, 6654–6659.
47 R. Car and M. Parrinello, Unified Approach for Molecular Dynamics and Density-Functional Theory, *Phys. Rev. Lett.*, 1985, **55**, 2471–2474.
48 W. Kohn and L. J. Sham, Self-Consistent Equations Including Exchange and Correlation Effects, *Phys. Rev.*, 1965, **140**, A1133–A1138.

49 N. Troullier and J. L. Martins, Efficient pseudopotentials for plane-wave calculations, *Phys. Rev. B:Condens. Matter Mater. Phys.*, 1991, **43**, 1993–2006.
50 J. P. Perdew, K. Burke and M. Ernzerhof, Generalized Gradient Approximation Made Simple, *Phys. Rev. Lett.*, 1996, **77**, 3865–3868.
51 D. M. Bylander and L. Kleinman, Efficacious Form for Model Pseudopotentials, *Phys. Rev. Lett.*, 1982, **48**, 1425–1428.
52 D. J. Evans and B. L. Holian, The Nose–Hoover thermostat, *J. Chem. Phys.*, 1985, **83**, 4069–4074.
53 W. Humphrey, A. Dalke and K. Schulten, VMD: visual molecular dynamics, *J. Mol. Graphics*, 1996, **14**, 33–38.
54 H. Wang, X. Kou, J. Zhang and J. Li, Large scale synthesis and characterization of Ni nanoparticles by solution reduction method, *Bull. Mater. Sci.*, 2008, **31**, 97–100.
55 N. A. Dhas, C. P. Raj and A. Gedanken, Synthesis, characterization, and properties of metallic copper nanoparticles, *Chem. Mater.*, 1998, **10**, 1446–1452.
56 Q. T. Trinh, A. Banerjee, Y. Yang and S. H. Mushrif, Sub-Surface Boron-Doped Copper for Methane Activation and Coupling: First-Principles Investigation of the Structure, Activity, and Selectivity of the Catalyst, *J. Phys. Chem. C*, 2017, **121**, 1099–1112.
57 J. Xu and M. Saeys, First principles study of the effect of carbon and boron on the activity of a Ni catalyst, *J. Phys. Chem. C*, 2009, **113**, 4099–4106.
58 G. Bussi and A. Laio, Using metadynamics to explore complex free-energy landscapes, *Nat. Rev. Phys.*, 2020, **2**, 200–212.
59 A. Laio and M. Parrinello, Escaping free-energy minima, *Proc. Natl. Acad. Sci. U. S. A.*, 2002, **99**, 12562–12566.
60 A. Laio and F. L. Gervasio, Metadynamics: A method to simulate rare events and reconstruct the free energy in biophysics, chemistry and material science, *Rep. Prog. Phys.*, 2008, **71**, 126601.
61 Z. Fan, W. Weng, J. Zhou, D. Gu and W. Xiao, Catalytic decomposition of methane to produce hydrogen: A review, *J. Energy Chem.*, 2021, **58**, 415–430.
62 J. Zeng, *et al.*, Initial Steps in CH4Pyrolysis on Cu and Ni, *J. Phys. Chem. C*, 2021, **125**, 18665–18672.
63 O. Mohan, Shambhawi, A. A. Lapkin and S. H. Mushrif, Investigating methane dry reforming on Ni and B promoted Ni surfaces: DFT assisted microkinetic analysis and addressing the coking problem, *Catal. Sci. Technol.*, 2020, **10**, 6628–6643.
64 J. J. Varghese and S. H. Mushrif, First-principles investigation of the dissociation and coupling of methane on small copper clusters: Interplay of collision dynamics and geometric and electronic effects, *J. Chem. Phys.*, 2015, **142**, 184308.
65 K. Li, C. He, M. Jiao, Y. Wang and Z. Wu, A first-principles study on the role of hydrogen in early stage of graphene growth during the CH4 dissociation on Cu(1 1 1) and Ni(1 1 1) surfaces, *Carbon*, 2014, **74**, 255–265.
66 G. Gajewski and C. W. Pao, Ab initio calculations of the reaction pathways for methane decomposition over the Cu(111) surface, *J. Chem. Phys.*, 2011, **135**, 064707.
67 W. Zhang, P. Wu, Z. Li and J. Yang, First-principles thermodynamics of graphene growth on Cu surfaces, *J. Phys. Chem. C*, 2011, **115**, 17782–17787.
68 Y. Zhou, *et al.*, Dopant-induced electron localization drives CO2 reduction to C2 hydrocarbons, *Nat. Chem.*, 2018, **10**, 974–980.
69 X. Nie, *et al.*, Mechanistic Insight into C–C Coupling over Fe-Cu Bimetallic Catalysts in CO2 Hydrogenation, *J. Phys. Chem. C*, 2017, **121**, 13164–13174.
70 F. C. Schouten, O. L. J. Gijzeman and G. A. Bootsma, Interaction of methane with Ni(111) and Ni(100); diffusion of carbon into nickel through the (100) surface; An aes-leed study, *Surf. Sci.*, 1979, **87**, 1–12.
71 J. Xu and M. Saeys, Improving the coking resistance of Ni-based catalysts by promotion with subsurface boron, *J. Catal.*, 2006, **242**, 217–226.

